Many-body pseudopotential theory of excitons in InP and CdSe quantum dots

A. Franceschetti, H. Fu, L. W. Wang, and A. Zunger
National Renewable Energy Laboratory, Golden, Colorado 80401
(Received 15 October 1998)

We present a pseudopotential approach to the calculation of the excitonic spectrum of semiconductor quantum dots. Starting from a many-body expansion of the exciton wave functions in terms of single-substitution Slater determinants constructed from pseudopotential single-particle wave functions, our method permits an accurate and detailed treatment of the intraconfiguration electron-hole Coulomb and exchange interactions, while correlation effects can be included in a controlled fashion by allowing interconfiguration coupling. We calculate the exciton fine structure of InP and CdSe nanocrystals in the strong-confinement regime. We find a different size dependence for the electron-hole exchange interaction than previously assumed (i.e., R^{-2} instead of R^{-3}). Our calculated exciton fine structure is compared with recent experimental results obtained by size-selective optical spectroscopies. [S0163-1829(99)00227-1]

I. INTRODUCTION

The physics of excitons in *bulk semiconductors*[1] is governed by electron-hole *correlation* effects, which control the magnitude of the exciton radius and exciton binding energy. A departure from this picture, however, is expected for excitons in semiconductor *quantum dots*: as the size R of the quantum dot is reduced, the separation between single-particle energy levels increases at a faster rate than the electron-hole Coulomb energy. When the physical size of the quantum dot becomes smaller than the bulk exciton radius (strong-confinement limit), the electron-hole correlation energy becomes negligible compared to the direct electron-hole Coulomb and exchange energies. Thus, the spectroscopy of strongly-confined quantum dots is decided by the hierarchy: Coulomb greater than exchange greater than correlation. In this paper we present a practical and accurate technique for calculating the excitonic spectrum of quantum dots that is designed for such cases.

Semiconductor nanocrystals in the strong-confinement regime can now be produced with a high degree of control over size and shape distributions.[2] In the case of CdSe,[3] InP,[4] and InAs,[5] the good quality of the nanocrystal samples has permitted one to resolve and identify several excitonic lines in the photoluminescence excitation (PLE) spectrum, spanning a range of more than 1 eV above the fundamental optical gap. By varying the PLE detection energy and/or the average size of the nanocrystals, the size dependence of the excitonic energy levels has been observed and analyzed. Furthermore, a careful utilization of size-selective spectroscopic techniques[6,7] has permitted a thorough investigation of the fine structure of the lowest excitonic transitions, showing for example a $\sim$10-meV redshift of the emission line from the lowest-energy absorption line.[6–12] Recent advances in the spectroscopy of single nanocrystals[13] suggest that the fine structure of the band-edge excitons, as well as higher-energy transitions, can be addressed in the near future with unprecedented detail.

The ''coarse'' excitonic structure of semiconductor nanocrystals is usually interpreted in terms of single-particle energy gaps, to which the effects of the electron-hole Coulomb interaction are added as a perturbation. This approach has been very successful at describing the size dependence of the excitonic lines in CdSe,[14] InP,[15] and InAs,[16] nanocrystals. However, the interpretation of the exciton ''fine'' structure requires a more detailed treatment of the electron-hole interaction. This goal is achieved here by a many-body expansion of the exciton wave functions in terms of single-substitution Slater determinants constructed from pseudopotential single-particle wave functions.

The idea of a ''configuration-interaction'' expansion of the exciton wave functions is not new. It was introduced in the framework of the single-band effective-mass approximation by Hu, Lindberg, and Koch,[17] and later applied to the tight-binding approximation.[18–21] Recently, however, accurate pseudopotential calculations[22,23] have shown that the use of effective-mass envelope functions to estimate Coulomb and exchange integrals can lead to considerable errors. For instance, the electron-hole Coulomb energy of the lowest-energy exciton is underestimated by as much as 40% in small nanocrystals.[22] Furthermore, pseudopotential calculations have shown that the electron-hole exchange energy includes a long-range component[23] that was previously ignored.[6,8–10] These effects are fully included in the present calculation.

The fine structure of the lowest exciton states of CdSe nanocrystal was previously discussed[6,8,9] in terms of a model 8×8 electron-hole Hamiltonian. The Hamiltonian matrix elements were derived starting from single-particle effective-mass wave functions calculated for spherical nanocrystals having the cubic lattice structure. The warping of the valence band and the nonparabolicity of the conduction band were neglected, while crystal-field splitting effects and deviations from sphericity were treated in a perturbative fashion. The four highest valence states (Γ_{8v} symmetry) and the two lowest conduction states (Γ_{6c} symmetry) were included in the basis set for the calculation of the excitonic structure. Only the short-range part of the electron-hole exchange interaction was included in the calculations; the long-range exchange interaction was neglected. The lowest-energy exciton state of spherical nanocrystals was predicted to have an infinite radiative lifetime (''dark exciton''). While the solutions of this

model Hamiltonian fit well the observed redshift in CdSe nanocrystals,[6,8,9] for spherical zinc-blende quantum dots this model predicts a $1/R^3$ scaling of the redshift with size,[9] which is not observed in either InP (Ref. 7) or InAs (Ref. 12) nanocrystals, where a $\sim 1/R^2$ scaling is seen instead.

More recently, a configuration-interaction approach based on a tight-binding parametrization of the bulk band structure was applied to CdSe nanocrystals by Leung, Pokrant, and Whaley.[20] The single-particle wave functions of CdSe nanocrystals in the wurtzite structure were calculated using a $\{s,p_x,p_y,p_z,s^*\}$ tight-binding basis set. The interaction parameters were derived from the band structure of the zinc-blende phase and adjusted to reproduce the wurtzite bulk band structure. Spin-orbit coupling was then added as a perturbation to the single-particle states. A configuration-interaction expansion of the exciton wave functions was performed, including both Coulomb and exchange matrix elements. The calculated redshift was in relatively good agreement with the experimental results of Efros *et al.*[9] A finite radiative lifetime of about 10^{-5} s was predicted for the lowest exciton state of spherical CdSe nanocrystals.

Our approach differs from previous calculations in that: (i) Crystal-field splitting, spin-orbit coupling, and shape effects are built at the outset into the solution of the single-particle Schrödinger equation and are not treated perturbatively. (ii) Microscopic pseudopotential wave functions (rather than envelope functions or tight-binding orbitals) are used to calculate the Coulomb and exchange matrix elements. (iii) A physically complete (albeit phenomenological) dielectric function is used to screen the electron-hole interaction; the dielectric function depends on the electron-hole separation as well as the quantum-dot size. (iv) Several configurations are included in the many-body expansion of the exciton wave functions. Thus, correlation effects can be described in a systematic and controlled fashion.

II. METHOD

The first step in the calculation of the excitonic structure of a nanocrystal is the solution of the single-particle problem. In the pseudopotential approach this amounts to solving the single-particle Schrödinger equation

$$\left[-\frac{\hbar^2}{2m_0}\nabla^2+V_{\rm ps}(\mathbf{r})+\hat{V}_{\rm nl}\right]\psi_i(\mathbf{r},\sigma)=\varepsilon_i\psi_i(\mathbf{r},\sigma), \tag{1}$$

where $V_{\rm ps}(\mathbf{r})$ is the microscopic pseudopotential of the system (dot plus surrounding material), and $\hat{V}_{\rm nl}$ is a short-range operator that accounts for the nonlocal part of the potential (including spin-orbit coupling). $V_{\rm ps}(\mathbf{r})$ is calculated here from the superposition of screened atomic potentials,

$$V_{\rm ps}(\mathbf{r})=\sum_{i,\alpha} v_\alpha(\mathbf{r}-\mathbf{R}_{i,\alpha}), \tag{2}$$

where $v_\alpha(\mathbf{r}-\mathbf{R}_{i,\alpha})$ is the atomic potential for an atom of type α located at the position $\mathbf{R}_{i,\alpha}$. The atomic pseudopotentials are derived from the bulk screened pseudopotential obtained in the framework of density-functional theory and are fitted to reproduce the measured bulk transition energies, deformation potentials, and effective masses.[24]

In the next step, from the solutions of Eq. (1) we construct a set of single-substitution Slater determinants $\{\Phi_{v,c}\}$, obtained from the ground-state Slater determinant Φ_0 by promoting an electron from the (occupied) valence state ψ_v of energy ε_v to the (unoccupied) conduction state ψ_c of energy ε_c:

$$\Phi_0(\mathbf{r}_1,\sigma_1,\ldots,\mathbf{r}_N,\sigma_N)=\mathcal{A}[\psi_1(\mathbf{r}_1,\sigma_1)\cdots\psi_v(\mathbf{r}_v,\sigma_v)\cdots\psi_N(\mathbf{r}_N,\sigma_N)], \tag{3a}$$

$$\Phi_{v,c}(\mathbf{r}_1,\sigma_1,\ldots,\mathbf{r}_N,\sigma_N)=\mathcal{A}[\psi_1(\mathbf{r}_1,\sigma_1)\cdots\psi_c(\mathbf{r}_v,\sigma_v)\cdots\psi_N(\mathbf{r}_N,\sigma_N)]. \tag{3b}$$

Here N is the total number of electrons in the system, $\sigma=\uparrow,\downarrow$ is the spin variable, and $\mathcal{A}$ is the antisymmetrizing operator. Two Slater determinants Φ_{v_1,c_1} and Φ_{v_2,c_2} belong to the same ''configuration'' if the single-particle valence states ψ_{v_1} and ψ_{v_2}, as well as the single-particle conduction states ψ_{c_1} and ψ_{c_2}, are degenerate: $\varepsilon_{v_1}=\varepsilon_{v_2}$ and $\varepsilon_{c_1}=\varepsilon_{c_2}$. Note that each single-particle level is at least twofold degenerate because of time-inversion symmetry (Kramer's doublet). As a result, each exciton configuration has a minimum dimension of four.

The exciton wave functions $\Psi^{(\alpha)}$ (where α denotes the exciton quantum numbers) are expanded in terms of this determinantal basis set,

$$\Psi^{(\alpha)}=\sum_{v=1}^{N_v}\sum_{c=1}^{N_c} C_{v,c}^{(\alpha)}\,\Phi_{v,c}, \tag{4}$$

where N_v and N_c denote the number of valence and conduction states included in the expansion of the exciton wave functions. In this notation the valence states are numbered from 1 to N_v in order of *decreasing* energy starting from the valence-band maximum, while the conduction states are numbered from 1 to N_c in order of *increasing* energy starting from the conduction-band minimum. Inclusion of multisubstitution Slater determinants will introduce additional multiexciton levels at higher energy. In this work we are interested only in single-exciton states; multiexciton states will be described in another publication.[25]

The matrix elements of the many-particle Hamiltonian $\mathcal{H}$ in the basis set $\{\Phi_{v,c}\}$ are calculated as

$$\mathcal{H}_{vc,v'c'}\equiv\langle\Phi_{v,c}|\mathcal{H}|\Phi_{v',c'}\rangle=(\epsilon_c-\epsilon_v)\,\delta_{v,v'}\delta_{c,c'}-J_{vc,v'c'}+K_{vc,v'c'}, \tag{5}$$

where J and K are the Coulomb and exchange integrals, respectively:

$$J_{vc,v'c'}=e^2\sum_{\sigma_1,\sigma_2}\int\int\frac{\psi^*_{v'}(\mathbf{r}_1,\sigma_1)\psi^*_c(\mathbf{r}_2,\sigma_2)\psi_v(\mathbf{r}_1,\sigma_1)\psi_{c'}(\mathbf{r}_2,\sigma_2)}{\bar{\epsilon}(\mathbf{r}_1,\mathbf{r}_2)|\mathbf{r}_1-\mathbf{r}_2|}d\mathbf{r}_1d\mathbf{r}_2, \tag{6}$$

$$K_{vc,v'c'}=e^2\sum_{\sigma_1,\sigma_2}\int\int\frac{\psi^*_{v'}(\mathbf{r}_1,\sigma_1)\psi^*_c(\mathbf{r}_2,\sigma_2)\psi_{c'}(\mathbf{r}_1,\sigma_1)\psi_v(\mathbf{r}_2,\sigma_2)}{\bar{\epsilon}(\mathbf{r}_1,\mathbf{r}_2)|\mathbf{r}_1-\mathbf{r}_2|}d\mathbf{r}_1d\mathbf{r}_2. \tag{7}$$

The screening of the electron-hole interaction, caused by the polarization of the medium, is described phenomenologically by the *microscopic*, position-dependent dielectric constant $\bar{\epsilon}$ and will be discussed in Sec. II B. The structure of the Hamiltonian matrix is schematically illustrated in Fig. 1. The diagonal blocks (shaded areas) correspond to matrix elements $\mathcal{H}_{vc,v'c'}$ between Slater determinants belonging to the same configuration. The off-diagonal blocks (unshaded areas) describe the coupling between different configurations.

The excitonic states of the quantum dot are obtained by solving the secular equation

$$\sum_{v'=1}^{N_v}\sum_{c'=1}^{N_c}\mathcal{H}_{vc,v'c'}C^{(\alpha)}_{v',c'}=E^{(\alpha)}C^{(\alpha)}_{v,c}. \tag{8}$$

From the knowledge of the exciton energy levels and wave functions, the near-edge normalized absorption spectrum can be obtained as

$$\sigma(\omega)\propto\frac{1}{V}\sum_{\alpha}|\mathbf{M}^{(\alpha)}|^2\delta(\hbar\omega-E^{(\alpha)}), \tag{9}$$

where V is the nanocrystal volume and $\mathbf{M}^{(\alpha)}$ are the dipole matrix elements:

$$\mathbf{M}^{(\alpha)}=\sum_{vc}C^{(\alpha)}_{v,c}\langle\psi_v|\mathbf{r}|\psi_c\rangle. \tag{10}$$

In the following sections the most important details of the solution of Eqs. (1)–(10) will be discussed.

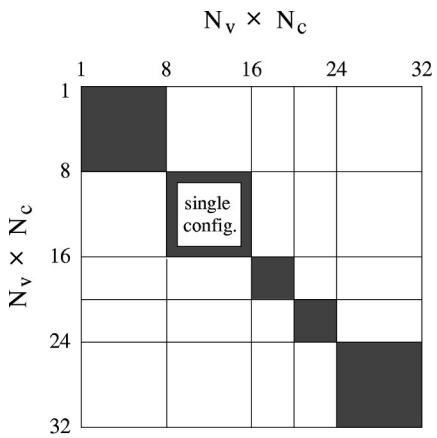

FIG. 1. Schematic form of the Hamiltonian matrix of Eq. (5). The shaded areas correspond to matrix elements between Slater determinants belonging to the same configuration.

A. Solution of the single-particle problem

The solution of the Schrödinger equation (1) for a 1000-atom system represents a formidable task, even when a fixed, non-self-consistent potential is used. However, only a few single-particle states in an energy window around the band gap are needed in the construction of the basis set $\{\Phi_{v,c}\}$. Thus, Eq. (1) can be effectively solved using the folded spectrum method,[26,27] which allows one to calculate *selected* eigenstates of the Schrödinger equation. In this approach, Eq. (1) is replaced by the eigenvalue equation

$$\left[-\frac{\hbar^2}{2m}\nabla^2+V_{\rm ps}(\mathbf{r})+\hat{V}_{\rm NL}-\varepsilon_{\rm ref}\right]^2\psi_i(\mathbf{r},\sigma)=(\varepsilon_i-\varepsilon_{\rm ref})^2\psi_i(\mathbf{r},\sigma), \tag{11}$$

where $\varepsilon_{\rm ref}$ is an *arbitrary* reference energy. The ''ground state'' of Eq. (11) coincides with the solution of the Schrödinger equation (1) with energy closest to the reference energy $\varepsilon_{\rm ref}$. Therefore, by choosing the reference energy in the band gap, the band-edge states can be obtained by minimizing the functional $A[\psi]=\langle\psi|(\hat{H}-\varepsilon_{\rm ref})^2|\psi\rangle$.

We solve Eq. (11) by expanding the pseudopotential wave functions $\psi_i(\mathbf{r},\sigma)$ in a plane-wave basis set. To this purpose, the total pseudopotential $V_{\rm ps}(\mathbf{r})$ is defined in a periodically repeated supercell Ω containing the quantum dot surrounded by a region of vacuum. The size of the vacuum region is sufficiently large to ensure that the solutions of Eq. (11) are converged within a few meV. The single-particle wave functions can then be expanded as $\psi_i(\mathbf{r},\sigma)=\Sigma_{\mathbf{G}}c_i(\mathbf{G},\sigma)\exp(i\mathbf{G}\cdot\mathbf{r})$, where the sum runs over the reciprocal-lattice vectors $\mathbf{G}$ of the supercell Ω. The energy cutoff of the plane-wave expansion is the same used to fit the bulk electronic structure, to ensure that the band structure consistently approaches the bulk limit. The minimization of the functional $A[\psi]$ is carried out in the plane-wave basis set using a preconditioned conjugate-gradients algorithm. More details on the minimization procedure, and the scaling with the system size can be found in Ref. 27.

B. Screening of Coulomb and exchange interactions

In the case of Wannier excitons in bulk semiconductors, the electron-hole *Coulomb* interaction is screened by the bulk dielectric constant. This fundamental result was derived for the first time to our knowledge by Sham and Rice[28] using effective-mass arguments. An alternative derivation was given by Strinati[29] using the GW approximation[30] for the electron self-energy. Pseudopotential calculations for semiconductor quantum dots[31] have shown that the macroscopic

dielectric constant decreases significantly as the size of the quantum dot is reduced, thus enhancing the electron-hole Coulomb energy.

The effects of dielectric screening on the electron-hole *exchange* interaction are more subtle. It is generally understood that in bulk semiconductors the short-range exchange interaction should be unscreened,[28,29] while the long-range exchange interaction should be screened by the bulk dielectric tensor.[32,33] Recent pseudopotential calculations for InP and CdSe nanocrystals[23] have revealed that the electron-hole exchange interaction in quantum-confined systems consists of a short-range component and a long-range component, which in the case of direct (Γ-derived) excitons have comparable magnitude. Therefore, the screening of the long-range exchange interaction has a sizable effect on the extent of the electron-hole exchange splitting in semiconductor quantum dots.

We will use here a position-dependent dielectric constant to screen the Coulomb and exchange interactions in quantum dots according to the electron-hole separation. The screened Coulomb potential of Eqs. (6) and (7) can be rewritten as

$$g(\mathbf{r}_1,\mathbf{r}_2)\equiv\frac{e^2}{\bar{\epsilon}(\mathbf{r}_1,\mathbf{r}_2)|\mathbf{r}_1-\mathbf{r}_2|}=e^2\int \epsilon^{-1}(\mathbf{r}_1,\mathbf{r})|\mathbf{r}-\mathbf{r}_2|^{-1}d\mathbf{r}, \tag{12}$$

where ϵ^{-1} is the inverse dielectric function. Assuming that $\epsilon^{-1}(\mathbf{r}_1,\mathbf{r})\approx\epsilon^{-1}(\mathbf{r}_1-\mathbf{r})$, the Fourier transform of the screened Coulomb potential is

$$g(\mathbf{k})=\epsilon^{-1}(\mathbf{k})\frac{4\pi e^2}{k^2}, \tag{13}$$

where $\epsilon^{-1}(\mathbf{k})$ is the Fourier transform of $\epsilon^{-1}(\mathbf{r}_1-\mathbf{r})$. The inverse dielectric constant $\epsilon^{-1}=\epsilon_{\rm el}^{-1}+\epsilon_{\rm ion}^{-1}$ consists of an electronic (high-frequency) contribution $\epsilon_{\rm el}^{-1}$ and an ionic (low-frequency) contribution $\Delta\epsilon_{\rm ion}^{-1}$, which are approximated here by the Thomas-Fermi model proposed by Resta[34] and by the polaronic model of Haken,[35] respectively. Both $\epsilon_{\rm el}^{-1}$ and $\Delta\epsilon_{\rm ion}^{-1}$ are diagonal and isotropic in reciprocal space, where they have the analytic form

$$\epsilon_{\rm el}^{-1}(k)=\frac{k^2+q^2\sin(k\rho_\infty)/(\epsilon_\infty^{\rm dot}k\rho_\infty)}{k^2+q^2}, \tag{14a}$$

$$\Delta\epsilon_{\rm ion}^{-1}(k)=\left(\frac{1}{\epsilon_0^{\rm dot}}-\frac{1}{\epsilon_\infty^{\rm dot}}\right)\left(\frac{1/2}{1+\rho_h^2k^2}+\frac{1/2}{1+\rho_e^2k^2}\right). \tag{14b}$$

Here $q=2\pi^{-1/2}(3\pi^2n_0)^{1/3}$ is the Thomas-Fermi wave vector (where n_0 is the electron density), and ρ_∞ is the solution of the equation $\sinh(q\rho_\infty)/(q\rho_\infty)=\epsilon_\infty^{\rm dot}$. Also, $\rho_{h,e}=(\hbar/2m_{h,e}\omega_{\rm LO})^{1/2}$, where $m_{h,e}$ denotes the hole (h) and electron (e) effective mass, and $\omega_{\rm LO}$ is the frequency of the bulk LO phonon mode. The *macroscopic* high-frequency and low-frequency dielectric constants of the quantum dot, $\epsilon_\infty^{\rm dot}$ and $\epsilon_0^{\rm dot}$, are related to the polarizability of the quantum dot as a whole. The high-frequency dielectric constant is obtained from a modified Penn model where the effective-mass band gap is replaced by the pseudopotential calculated band gap,

$$\epsilon_\infty^{\rm dot}(R)=1+(\epsilon_\infty^{\rm bulk}-1)\frac{[E_{\rm gap}^{\rm bulk}+\Delta E]^2}{[E_{\rm gap}^{\rm dot}(R)+\Delta E]^2}, \tag{15}$$

where $\epsilon_\infty^{\rm bulk}$ is the bulk high-frequency dielectric constant, and $E_{gap}^{\rm bulk}+\Delta E$ is the energy of the first pronounced peak in the bulk absorption spectrum (corresponding to the E_2 transition in zinc-blende semiconductors). The low-frequency dielectric constant is obtained as $\epsilon_0^{\rm dot}(R)=\epsilon_\infty^{\rm dot}(R)+(\epsilon_0^{\rm bulk}-\epsilon_\infty^{\rm bulk})$.

The electron-hole Coulomb interaction is long ranged, so it is essentially screened by the quantum-dot macroscopic dielectric constant. The electron-hole exchange interaction, on the other hand, consists of both a short-range and a long-range component.[23] Since $\bar{\epsilon}(\mathbf{r}_1-\mathbf{r}_2)\to1$ when $|\mathbf{r}_1-\mathbf{r}_2|\to0$, the short-range component of the exchange interaction is effectively unscreened, as it is in bulk semiconductors.[28,32,33] The long-range component, instead, is significantly screened, as discussed in detail in Ref. 23.

Unlike the dielectric constants used in previous effective-mass[8,9] and tight-binding[18–21] calculations, our dielectric function depends both on the electron-hole separation and the quantum-dot size. In previous calculations the electron-hole exchange interaction was either left unscreened[9,19,21] or screened by the *bulk* distance-dependent dielectric constant.[18,20]

C. Calculation of Coulomb and exchange integrals

The Coulomb [Eq. (6)] and exchange [Eq. (7)] integrals can be cast in the general form

$$\int\int \rho_1^*(\mathbf{r})g(\mathbf{r}-\mathbf{r}')\rho_2(\mathbf{r}')d\mathbf{r}d\mathbf{r}'=\int \rho_1^*(\mathbf{r})\phi_2(\mathbf{r})d\mathbf{r}, \tag{16}$$

where $\rho_1(\mathbf{r})$ and $\rho_2(\mathbf{r})$ denote products of complex single-particle wave functions and include a sum over the spin variable σ [see Eqs. (6) and (7)].

The screened electrostatic potential $\phi_2(\mathbf{r})=\int g(\mathbf{r}-\mathbf{r}')\rho_2(\mathbf{r}')d\mathbf{r}'$ is conveniently calculated in reciprocal space using the convolution theorem; we have

$$\phi_2(\mathbf{r})=\sum_{\mathbf{G}} g(\mathbf{G})\rho_2(\mathbf{G})e^{i\mathbf{G}\cdot\mathbf{r}}, \tag{17}$$

where $g(\mathbf{G})$ and $\rho_2(\mathbf{G})$ are the Fourier transforms of $g(\mathbf{r})$ and $\rho_2(\mathbf{r})$, respectively. Compared to the real-space computation[22] of ϕ_2, the reciprocal-space formalism offers a higher degree of flexibility in dealing with different functional forms of the screening function $g(\mathbf{r})$ and different geometries of the supercell Ω. However, the use of periodic boundary conditions in the calculation of ϕ_2 introduces spurious *electrostatic* interactions between periodic replicas of the quantum dot, even when the supercell Ω is sufficiently large to ensure that the quantum dots are electronically decoupled. A practical and effective way to overcome this difficulty is discussed in the Appendix.

III. EXCITONIC ENERGY LEVELS

We consider here nearly spherical InP and CdSe nanocrystals. The InP nanocrystals have the zinc-blende crystalline

TABLE I. Near-edge single-particle states of InP and CdSe spherical nanocrystals. For each value of the nanocrystal radius, the first row gives the energy (in eV) of the single-particle states with respect to the vacuum level, while the second row indicates the symmetry of the bulk Bloch states from which the nanocrystal states originate, as well as the dominant angular momentum character of their envelope function. The symbols $h1,\ldots,h4$ denote the four highest-energy valence-band levels, while $e1$,$e2$ denote the two lowest-energy conduction-band levels.

Dot radius (Å)	$h1$	$h2$	$h3$	$h4$	$e1$	$e2$
ZB InP						
10.11	-6.390	-6.390	-6.499	-6.563	-3.568	-3.225
	Γ_{8v}, s-like	Γ_{8v}, s-like	Γ_{7v}, s-like	Γ_{8v}, p-like	Γ_{6c}, s-like	L_{6c}, s-like
11.84	-6.319	-6.319	-6.364	-6.364	-3.726	-3.378
	Γ_{8v}, s-like	Γ_{8v}, s-like	Γ_{8v}, p-like	Γ_{8v}, p-like	Γ_{6c}, s-like	L_{6c}, s-like
14.00	-6.148	-6.148	-6.237	-6.237	-3.744	-3.481
	Γ_{8v}, s-like	Γ_{8v}, s-like	Γ_{8v}, p-like	Γ_{8v}, p-like	Γ_{6c}, s-like	L_{6c}, s-like
17.39	-6.092	-6.092	-6.145	-6.145	-3.968	-3.660
	Γ_{8v}, s-like	Γ_{8v}, s-like	Γ_{8v}, p-like	Γ_{8v}, p-like	Γ_{6c}, s-like	L_{6c}, s-like
WZ CdSe						
10.33	-5.904	-5.947	-5.987	-5.998	-2.901	-2.282
	Γ_{8v}, s-like	Γ_{8v}, s-like	Γ_{8v}, p-like	Γ_{8v}, p-like	Γ_{6c}, s-like	Γ_{6c}, p-like
14.63	-5.691	-5.719	-5.741	-5.747	-3.178	-2.765
	Γ_{8v}, s-like	Γ_{8v}, s-like	Γ_{8v}, p-like	Γ_{8v}, p-like	Γ_{6c}, s-like	Γ_{6c}, p-like
19.24	-5.561	-5.589	-5.599	-5.602	-3.319	-3.020
	Γ_{8v}, s-like	Γ_{8v}, s-like	Γ_{8v}, p-like	Γ_{8v}, p-like	Γ_{6c}, s-like	Γ_{6c}, p-like

structure and their overall symmetry is T_d. The CdSe nanocrystals have the wurtzite crystalline structure. In both cases, the interatomic distance is taken as the experimental bulk interatomic distance. The dangling bonds at the surface of the nanocrystals are passivated by ligandlike potentials, which are designed to remove the surface states from the band gap and minimize the coupling with the band-edge states. Crystal-field and spin-orbit effects, which previously were treated perturbatively,[8,9,20,21] are described here explicitly by specifying the atomic positions and the nonlocal potentials.

The effective radius of the nanocrystals is defined in terms of the number of atoms in the dot ($N_{\rm dot}$) as $R=a_0(\gamma N_{\rm dot})^{1/3}$, where a_0 is the bulk lattice constant, $\gamma=3/32\pi$ for zinc-blende dots, and $\gamma=3\sqrt{3}c_0/32\pi a_0$ for wurtzite dots. The nanocrystals considered here have effective diameter ranging from $\sim$20–40 Å.

The calculation of the single-particle energies and wave functions was discussed in detail by Wang and Zunger[14] for CdSe nanocrystals and by Fu and Zunger[15] for InP nanocrystals. Table I summarizes the energy and the wave-function character of a few near-edge single-particle states for the nanocrystals considered in this work. Each energy level in Table I is doubly degenerate, due to time-inversion symmetry. The two highest occupied energy levels (denoted as h_1 and h_2 in Table I) derive primarily from the bulk Γ_{8v} states and have an s-like envelope function. These two energy levels are degenerate in T_d-symmetry InP nanocrystals, while they are split by crystal-field and shape effects in wurtzite CdSe nanocrystals. The next two occupied energy levels (h_3 and h_4) also derive from the bulk Γ_{8v} states but have a p-like envelope function (with the exception of the $R=10.11$ Å InP nanocrystal, where the h_3 level originates from the Γ_{7v} split-off state). The lowest unoccupied energy level (denoted as $e1$ in Table I) derives from the bulk Γ_{6c} state and has an s-like envelope function. The next unoccupied energy level ($e2$) is L_{6c} derived in InP nanocrystals and Γ_{6c} derived in CdSe nanocrystals.

In what follows, we will examine the evolution of the excitonic spectrum as more detailed electron-hole interactions are included: single-particle energy differences, diagonal electron-hole Coulomb interaction, single-configuration approach (including intraconfiguration Coulomb and exchange integrals), and finally configuration interaction (including interconfiguration coupling).

A. Single-particle spectrum

If the electron-hole interaction is neglected, the exciton wave functions are given simply by the Slater determinants $\{\Phi_{v,c}\}$, corresponding to noninteracting electron-hole pairs of energy $\varepsilon_c-\varepsilon_v$ [see Eq. (5)]. Note that at this level of approximation all the excitonic states originating from the same single configuration are degenerate. The single-particle spectrum of a few InP and CdSe nanocrystals is shown in Fig. 2 (left-hand column). The excitonic levels are labeled according to the electron-hole pairs (hi,ej) from which they originate. The two lowest excitonic levels correspond to the ($h1$,$e1$) and ($h2$,$e2$) electron-hole pairs (which are energetically degenerate in InP nanocrystals) and are optically active (large oscillator strength). The next two excitonic levels correspond to the ($h3$,$e1$) and ($h4$,$e1$) electron-hole pairs and are optically inactive (small oscillator strength) because of the different symmetry of the electron and hole envelope

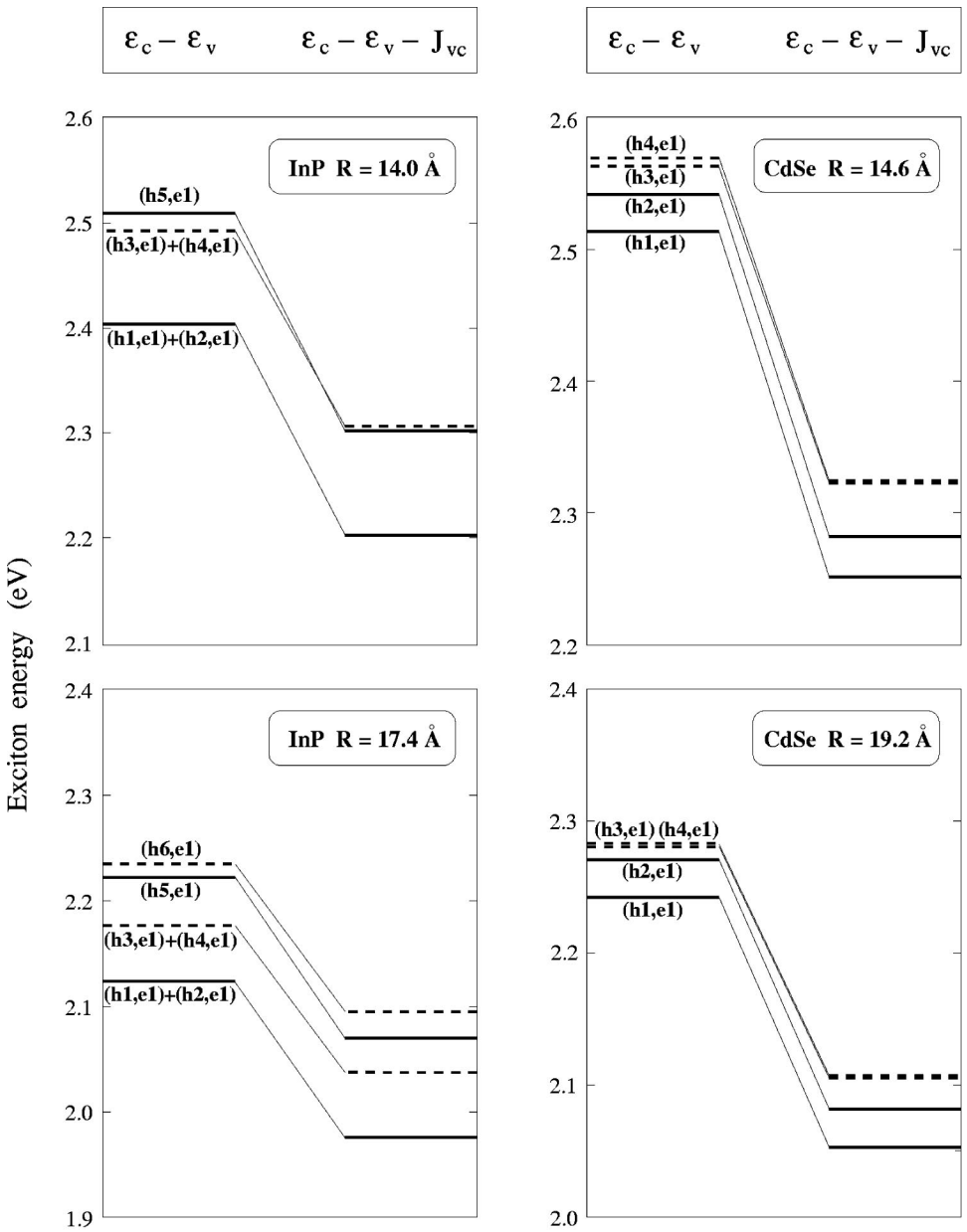

FIG. 2. Single-particle exciton levels of InP and CdSe nanocrystals with and without diagonal Coulomb energy. The symbols in parentheses denote the electron-hole pairs from which the exciton states originate. Solid lines correspond to optically active states (large oscillator strength), while dashed lines correspond to optically inactive states (small oscillator strength).

functions (see Table I). The $(h5,e1)$ electron-hole pair of InP nanocrystals is optically active, as shown in Fig. 2, because the $h5$ single-particle state originates mainly from the Γ_{7v} bulk state and has an *s*-like envelope function.

B. Diagonal Coulomb energy

The effects of the electron-hole Coulomb interaction on the excitonic energy levels of a nanocrystal can be approximated using first-order perturbation theory. The excitonic levels are then given by $\varepsilon_c - \varepsilon_v - J_{v,c}$, where $J_{v,c}$ are the *diagonal* electron-hole Coulomb energies $J_{v,c} \equiv J_{vc,vc}$.

In Ref. 22 we studied in detail the size dependence of the diagonal Coulomb energies $J_{v,c}$ using pseudopotential wave functions and compared our calculations with effective-mass results. It was found that for the lowest-energy excitonic state the unscreened Coulomb energy $J^o_{v,c}$ scales approximately as $R^{-0.8}$ with the size of the nanocrystal, and that the effective-mass approximation (which predicts a R^{-1} scaling) significantly overestimates the Coulomb energy.

The effects of the diagonal Coulomb energies on the excitonic spectrum are shown in Fig. 2 for InP and CdSe nanocrystals (right-hand column). The electron-hole Coulomb energy tends to lower the exciton energy levels, typically by 0.1–0.4 eV. Interestingly, the magnitude of the Coulomb energy is different for different energy levels, and in some cases this leads to level crossing. For example, the Coulomb energy of the $(h5,e1)$ electron-hole pair in the $R = 14.0$ Å InP nanocrystal is significantly larger than the Coulomb energy of the $(h3,e1)$ and $(h4,e1)$ pairs (0.207 eV versus 0.186 eV). Thus, although the $(h5,e1)$ pair is higher in energy than the $(h3,e1)$ and $(h4,e1)$ pairs

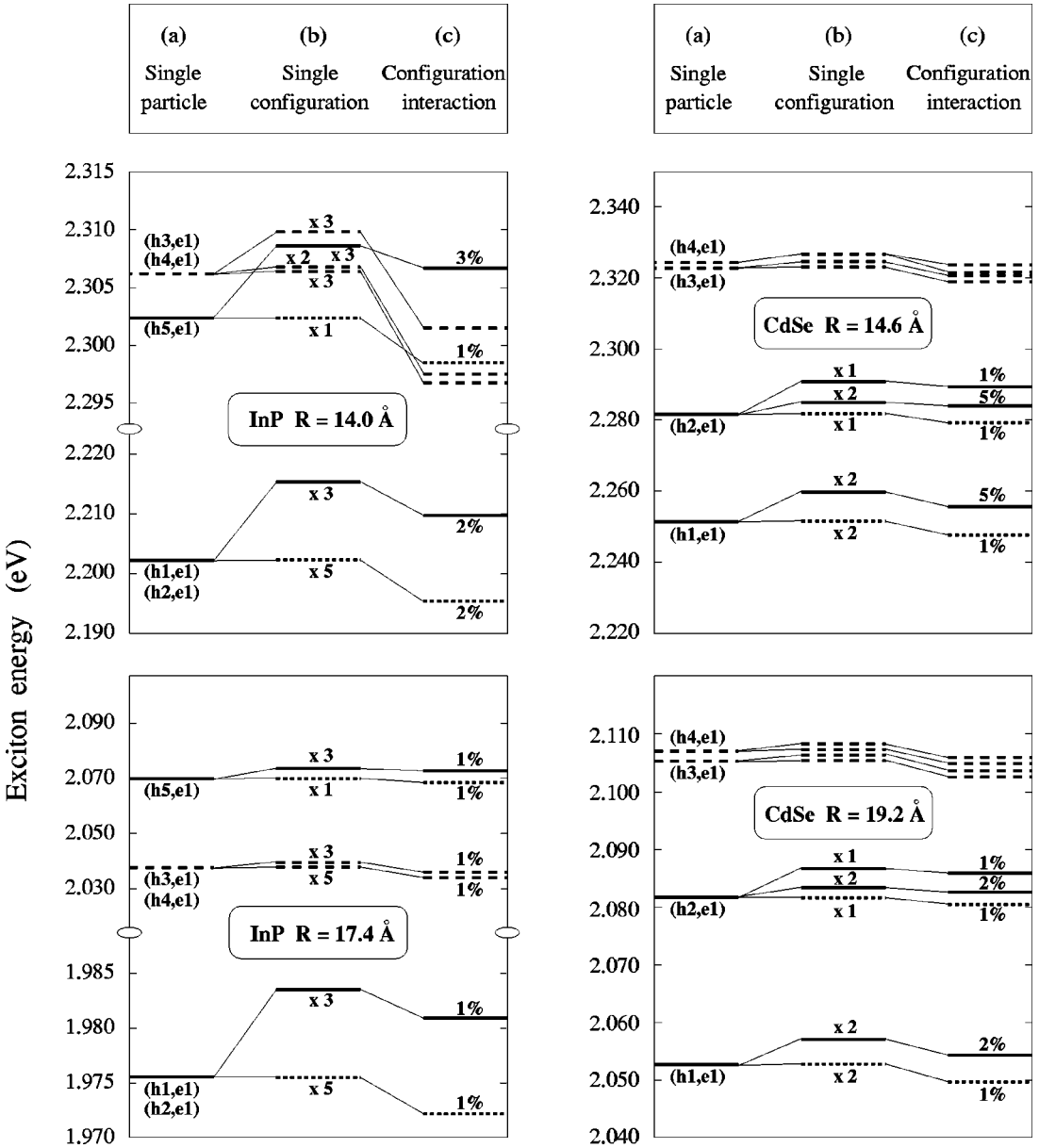

FIG. 3. (a) Single-particle spectrum of InP and CdSe nanocrystals including Coulomb interaction. (b) Single-configuration spectrum. (c) Configuration-interaction spectrum. Solid lines denote optically active states, dashed lines denote orbitally-forbidden states, dotted lines denote spin-forbidden states. The symbols in parentheses in (a) denote the electron-hole pairs from which the exciton states originate. The degeneracy of each exciton level in the single-configuration approximation is shown in (b). The configuration-mixing coefficients $\mathcal{R}^{(\alpha)}$ [see Eq. (18)] are shown in (c). The total number of single-particle states included in the configuration-interaction expansion is 26 valence states and 18 conduction states for the $R=14.0$ Å InP nanocrystal, 22 valence states and 10 conduction states for the $R=17.4$ Å InP nanocrystal, 8 valence states and 8 conduction states for the two CdSe nanocrystals.

in the single-particle approximation, the order is reversed when the Coulomb interaction is included (see Fig. 2).

C. Single-configuration approximation

In the ''single-configuration'' approach, only the diagonal blocks of the Hamiltonian matrix $\mathcal{H}_{vc,v'c'}$ (shaded areas in Fig. 1) are retained. The intraconfiguration Coulomb and exchange matrix elements are fully included in the single-configuration calculation, whereas the interaction between different configurations (nonshaded areas in Fig. 1) is neglected. This approach was used by Efros *et al.*[9] in the context of the $\mathbf{k}\cdot\mathbf{p}$ approximation to analyze the splitting of the lowest-energy exciton in CdSe nanocrystals.

The single-configuration spectrum of InP and CdSe nanocrystals is shown in Fig. 3(b). While the effects of the intraconfiguration Coulomb interaction are negligible, the exciton levels are split by the intraconfiguration exchange interaction into a lower-energy, spin-forbidden multiplet (dotted lines), and a higher-energy, spin-allowed multiplet (solid lines). This splitting creates the exciton ''fine structure.''

D. Configuration-interaction spectrum

In the final step, the configuration-interaction spectrum is obtained by diagonalizing the Hamiltonian matrix of Eq. (5). The convergence of the configuration-interaction expansion

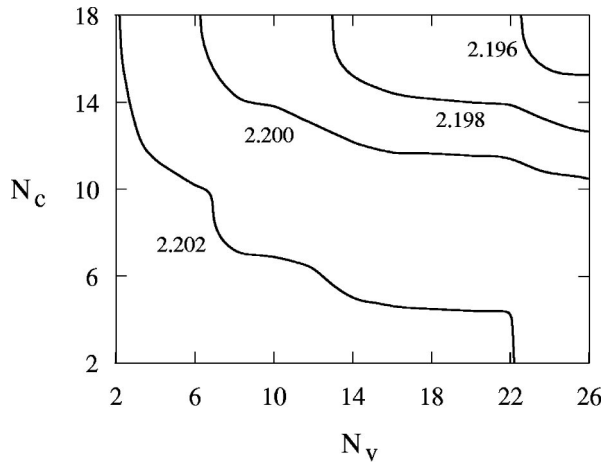

FIG. 4. Convergence of the lowest exciton energy with the number of valence-band states (N_v) and conduction-band states (N_c) included in the expansion of Eq. (4). The curves correspond to isolines with the same exciton energy.

in terms of the size of the determinantal basis set is illustrated in Fig. 4. This figure shows a contour plot of the lowest exciton energy of an InP nanocrystal ($R=14.0$ Å) as a function of the number of valence states (N_v) and conduction states (N_c) included in the many-body expansion of Eq. (4). As we can see from Fig. 4, the convergence of the exciton energy levels is quite slow. The convergence of the level splittings, however, is relatively fast. We estimate that the calculated exchange splitting of the lowest-energy exciton state is converged within 0.5 meV for the nanocrystals considered here. The splitting of higher-energy exciton states is converged within a few meV.

The extent of configuration mixing can be quantified by defining the mixing coefficient

$$\mathcal{R}^{(\alpha)}=1-\sum_{v,c}|C_{v,c}^{(\alpha)}|^2, \tag{18}$$

where the sum is restricted to the Slater determinants belonging to the single configuration from which the exciton state $\Psi^{(\alpha)}$ predominantly originates. The energy spectrum including configuration-interaction effects is shown in Fig. 3(c). The main consequence of configuration mixing is a significant downshift (several meV) of the energy levels. In some cases level crossing can be observed, although the configuration mixing is relatively small ($\mathcal{R}^{(\alpha)}\leqslant 5\%$ in all the cases considered here). Interestingly, we find that the lowest excitonic state is essentially spin forbidden, even when configuration mixing is included. In fact, the ratio between the transition probabilities of the lowest allowed transition and the lowest forbidden transition is at least 10^6 in CdSe nanocrystals and 10^{10} in InP nanocrystals. This is in contrast with the results of Leung *et al.*[20] who found a ratio of about 10^3 in the case of CdSe spherical nanocrystals. The allowed/forbidden ratio may depend strongly on the shape of the nanocrystal.

IV. ANALYSIS OF THE BAND-EDGE EXCITON LEVELS

A. Exciton energies

In a semiconductor nanocrystal with T_d symmetry the Γ_{8v} valence-band maximum is four-fold degenerate, while the Γ_{6c} conduction-band minimum is twofold degenerate (including spin degeneracy). Thus, in the absence of electron-hole interaction, the lowest exciton level is eightfold degenerate. This degeneracy can be broken by deviations from the T_d symmetry and/or by the electron-hole interaction.

Using a perturbative approach (which neglects configuration interactions), Efros *et al.*[9] have shown that the lowest exciton eightfold multiplet splits into five different energy levels, which are labeled (subscripts) according to their total angular momentum projection F:

$$\begin{aligned}
E_{\pm 2}&=-\frac{3}{2}\Delta_X-\frac{1}{2}\Delta_{\mathrm{CF}},\\
E_{\pm 1}^{L}&=\frac{1}{2}\Delta_X-\sqrt{\frac{(2\Delta_X-\Delta_{\mathrm{CF}})^2}{4}+3\Delta_X^2},\\
E_{\pm 1}^{U}&=\frac{1}{2}\Delta_X+\sqrt{\frac{(2\Delta_X-\Delta_{\mathrm{CF}})^2}{4}+3\Delta_X^2},\\
E_{0}^{L}&=-\frac{3}{2}\Delta_X+\frac{1}{2}\Delta_{\mathrm{CF}},\\
E_{0}^{U}&=\frac{5}{2}\Delta_X+\frac{1}{2}\Delta_{\mathrm{CF}},
\end{aligned} \tag{19}$$

where Δ_X is the exchange parameter, and Δ_{CF} is a perturbative parameter that accounts for deviations from the T_d symmetry (due to crystal-field splitting and/or deviations from sphericity). Both Δ_X and Δ_{CF} depend, in general, on the nanocrystal size.

In the case of spherical InP nanocrystals, the T_d symmetry is preserved, and $\Delta_{\mathrm{CF}}=0$. Thus, according to Eq. (19), the original eight-fold multiplet splits into a quintuplet with energy $E_{\mathrm{quint}}=-3\Delta_X/2$ and a triplet with energy $E_{\mathrm{triplet}}=5\Delta_X/2$. Since $\Delta_X>0$, the triplet lies above the quintuplet, and the exciton exchange splitting is given by $\Delta E_x=E_{\mathrm{triplet}}-E_{\mathrm{quint}}=4\Delta_X$. The triplet states are optically active, while the quintuplet states are optically inactive; thus, the exciton splitting ΔE_x corresponds to a redshift of the lowest emission line with respect to the lowest absorption line.

In the case of CdSe nanocrystals, the T_d symmetry is broken by the wurtzite lattice structure (even for spherical nanocrystals), and $\Delta_{\mathrm{CF}}>0$. Thus, the five energy levels of Eq. (19) are, in general, nondegenerate. The lowest-energy excitonic level is the optically inactive doublet $E_{\pm 2}$, while the next excitonic level is the optically active doublet $E_{\pm 1}^{L}$. The redshift of the emission line with respect to the absorption line is then given by $\Delta E_x=E_{\pm 1}^{L}-E_{\pm 2}$.

Our pseudopotential many-body expansion allows us to obtain $\Delta_X(R)$ and $\Delta_{\mathrm{CF}}(R)$ from first principles. For T_d-symmetry InP nanocrystals $\Delta_{\mathrm{CF}}=0$, and Δ_X is derived directly from the exchange splitting, $\Delta_X=\Delta E_x/4$. For CdSe nanocrystals the crystal-field splitting parameter Δ_{CF} is given by the difference between the energies of the $h1$ and $h2$ single-particle levels (see Table I). The exchange parameter Δ_X is then fitted to reproduce the calculated exciton energy levels according to Eq. (19). The quality of the fit is quite good, the average error in the exciton energies being about 1

TABLE II. Crystal-field splitting parameter Δ_{CF} and exchange parameter Δ_X of InP and CdSe nanocrystals calculated using the configuration-interaction approach. Also shown is the short-range exchange parameter Δ_X^{EMA} obtained by Efros *et al.* (Ref. 9) using the effective-mass approximation.

Dot radius (Å)	Δ_{CF} (meV)	Δ_X (meV)	Δ_X^{EMA} (meV)
ZB InP			
10.11	0	5.75	
11.84	0	4.68	
14.00	0	3.58	
17.39	0	2.16	
WZ CdSe			
10.32	43.3	5.53	16.20
14.63	28.3	2.91	5.69
19.24	28.7	1.51	2.50

meV. Our results are summarized in Table II. We next compare our results with previous calculations and with experiment.

B. Comparison with previous calculations

In the phenomenological approach used by Norris *et al.*,[6] Nirmal *et al.*,[8] Efros *et al.*,[9] Chamarro *et al.*,[10] and Woggon *et al.*,[11] the exchange parameter Δ_X was calculated retaining only the short-range part of the electron-hole exchange interaction and, therefore, assuming that the exchange parameter scales as $1/R^3$ with the nanocrystal size. Also, the crystal-field contribution to Δ_{CF} was assumed to be size independent.

The last column of Table II shows the exchange parameter Δ_X^{EMA} for CdSe nanocrystals, calculated according to the effective-mass model of Efros *et al.*[9] We see that Δ_X^{EMA} is significantly overestimated compared to the direct pseudopotential calculation. By fitting the *size dependence* of our calculated exchange energy with the functional form $\Delta_X(R) = aR^{-\gamma}$, we obtain $\gamma = 1.93$ for InP nanocrystals[36] and $\gamma = 1.97$ for CdSe nanocrystals. This is in contrast with the conventional assumption[6,8–10] that Δ_X scales as R^{-3}. The reason for this discrepancy is the presence of a sizable long-range component in the electron-hole exchange interaction.[23] Banin *et al.*[12] found experimentally that the exchange splitting in InAs nanocrystals scales approximately as R^{-2}. They interpreted their results in the framework of the effective-mass approximation by assuming the existence of a significant leakage of the electron wave function outside the nanocrystal. The resulting exchange parameter was then multiplied by an adjustable prefactor and fitted to the experimental exchange splitting. This model, however, ignores the long-range contributions to Δ_X, which are responsible for the R^{-2} scaling.

C. Comparison with experiment

The exciton splitting of InP nanocrystals calculated using pseudopotential wave functions is compared in Fig. 5 with a fit to the experimental results of Micic *et al.*[7] As we can see, the agreement with experimental results is very good and

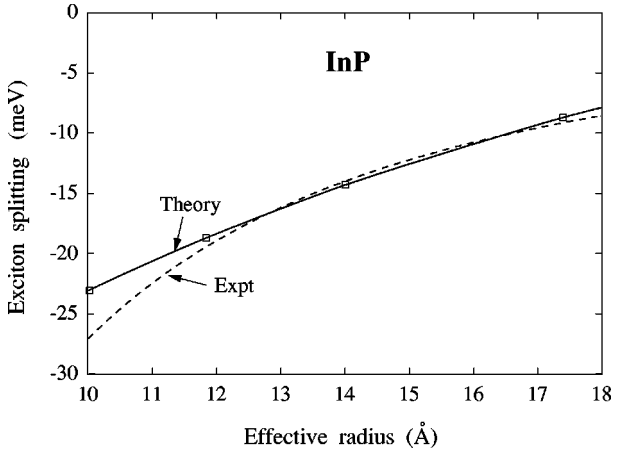

FIG. 5. The pseudopotential calculated exciton splitting of spherical InP nanocrystals (solid line) is compared with a fit to the experimental results of Micic *et al.* (Ref. 7, dashed line). The energy of the lowest spin-allowed optical transition is taken as the zero of the energy scale.

indicates that the observed redshift of the emission peak originates from the exciton exchange splitting.

Figure 6 compares the calculated low-energy excitonic levels of CdSe nanocrystals with the experimental results of Norris *et al.*[6] The exciton energies are plotted as a function of the band-gap energy (corresponding to the energy of the lowest absorbing state), as the measured nanocrystal size is subject to significant uncertainty. The two exciton levels $E_{\pm 1}^U$ and E_0^U are not resolved experimentally for small nanocrystals (band gap >2.1 eV), so their average is shown in Fig. 6. The agreement between theory and experiment is very good, although some discrepancies seem to exist for large nanocrystals (band gap $\leqslant 2$ eV). We observe, however, that in the bulk limit the exciton levels $E_{\pm 2}$ and $E_{\pm 1}^L$ should converge to $E=0$, while the levels E_0^L, $E_{\pm 1}^U$, and E_0^U should

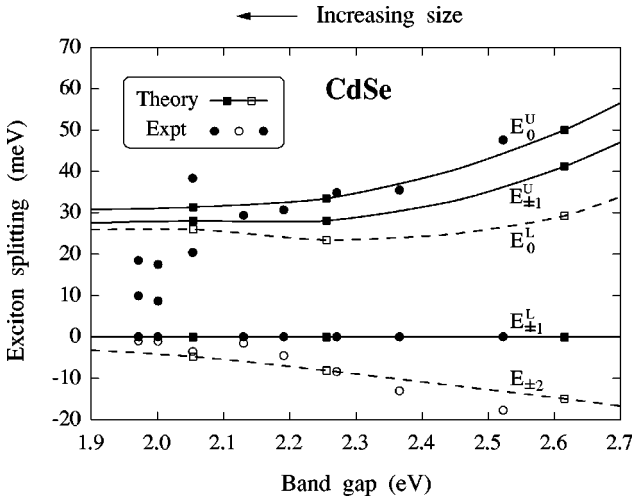

FIG. 6. Comparison of calculated (squares joined by lines) and measured (circles) excitonic levels of CdSe nanocrystals as a function of the band-gap energy. The experimental results are taken from Ref. 6. Solid symbols and solid lines denote optically active states, while open symbols and dashed lines denote optically inactive states. The energy of the lowest spin-allowed optical transition ($E_{\pm 1}^L$) is taken as the zero of the energy scale.

converge to the value of the bulk crystal-field splitting, $E = 26$ meV. The experimental exciton energies for large nanocrystals do not appear to approach the bulk limit in a consistent way.

V. SUMMARY

Using a many-body expansion based on *microscopic* pseudopotential wave functions, we have developed a practical and accurate method to calculate the excitonic spectrum of semiconductor quantum dots in the strong-confinement regime. We find that (i) the diagonal Coulomb energies $J_{v,c}$ depend on the electron and hole orbitals. This effect leads in some cases to level crossing (Fig. 2). (ii) Intraconfiguration exchange leads to splitting into spin-forbidden and spin-allowed multiplets (Fig. 3). (iii) Configuration mixing leads to significant energy lowering and possibly to state crossing (Fig. 3). If configuration interactions are ignored, the excitonic energy levels are off by several meV. (iv) Configuration mixing does not significantly affect the oscillator strength of the lowest, spin-forbidden excitonic multiplet. (v) The phenomenological single-configuration model of Efros *et al.*[9] is analyzed. We find that the exchange parameter $\Delta_X(R)$ has a different size dependence than previously assumed.[9]

ACKNOWLEDGMENTS

This work was supported by the U.S. DOE, OER-BES, Division of Materials Science, under Grant No. DE-AC36-98-GO 10337.

APPENDIX

In this appendix we discuss a practical and accurate method to accelerate the convergence of the reciprocal-space expansion of Coulomb [Eq. (6)] and exchange [Eq. (7)] integrals with respect to the volume Ω of the supercell containing the quantum dot and the surrounding barrier. In the reciprocal-space formalism [see Eqs. (16) and (17)], these integrals have the general form

$$E(\Omega)=\sum_{\mathbf{G}} \rho_1^*(\mathbf{G})g(\mathbf{G})\rho_2(\mathbf{G}), \tag{A1}$$

where $\rho_1(\mathbf{G})$, $\rho_2(\mathbf{G})$, and $g(\mathbf{G})$ are the Fourier transforms of $\rho_1(\mathbf{r})$, $\rho_2(\mathbf{r})$, and $g(\mathbf{r}-\mathbf{r}')$, respectively, and the sum runs over the reciprocal-lattice vectors $\mathbf{G}$ of the supercell Ω.

The convergence of the Fourier expansion (A1) with the supercell volume Ω is decided by the lowest-order multipole moments of ρ_1 and ρ_2. In order to accelerate the convergence, we subtract the multipole contributions from $E(\Omega)$ to obtain a *corrected* energy integral $\tilde{E}(\Omega)$, which approaches the converged value $E(\infty)\equiv\tilde{E}(\infty)$ at a much faster rate. Our approach is a generalization of the method developed by Makov and Payne[37] in the context of *ab initio* calculations for finite systems using periodic boundary conditions.

The lowest-order multipole moments of ρ_1 and ρ_2 are

$$\text{monopole:}\quad q_{1,2}=\int \rho_{1,2}(\mathbf{r})d\mathbf{r},$$

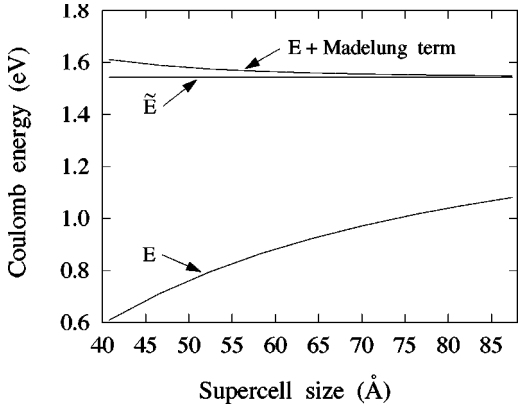

FIG. 7. Convergence of the unscreened diagonal Coulomb energy $J^0_{v,c}$ between the valence-band maximum and the conduction-band minimum of an InP nanocrystal ($R=14.0$ Å), as a function of the supercell size. The curve labeled E corresponds to the uncorrected Coulomb integral of Eq. (A1), $\tilde{E}$ is the corrected Coulomb integral of Eq. (A3), and (E + Madelung term) corresponds to Eq. (A3) where only the first correction term is retained.

$$\text{dipole:}\quad \mathbf{D}_{1,2}=\int \rho_{1,2}(\mathbf{r})\mathbf{r}d\mathbf{r}, \tag{A2}$$

$$\text{quadrupole:}\quad Q_{1,2}=\int \rho_{1,2}(\mathbf{r})r^2 d\mathbf{r}.$$

Because of the particular form of ρ_1 and ρ_2 [see Eqs. (6) and (7)], the monopole moments q_1 and q_2 can only take the values 0 and 1. Note that for a finite system the dipole and quadrupole moments are well defined and independent of the choice of the supercell Ω, provided that $\rho_1(\mathbf{r})$ and $\rho_2(\mathbf{r})$ vanish at the boundaries of the supercell.

The corrected form of $E(\Omega)$ is then obtained (see Ref. 37) as

$$\tilde{E}(\Omega)=E(\Omega)-\frac{q_1q_2}{\epsilon_0^{\text{dot}}}a_{\text{mad}}+\frac{4\pi}{3\Omega\epsilon_0^{\text{dot}}}\mathbf{D}_1\cdot\mathbf{D}_2$$

$$-\frac{2\pi}{3\Omega\epsilon_0^{\text{dot}}}(q_1Q_2+q_2Q_1), \tag{A3}$$

where the Madelung parameter a_{mad} is given by the Ewald sum[38]

$$a_{\text{mad}}=\sum_{\mathbf{R}\neq 0}\frac{\text{erfc}(R\eta^{1/2})}{R}+\frac{4\pi}{\Omega}\sum_{\mathbf{G}\neq 0}\frac{\exp(-G^2/4\eta)}{G^2}-\left(\frac{4\eta}{\pi}\right)^{1/2}$$

$$-\frac{\pi}{\eta\Omega}. \tag{A4}$$

Here η is the (arbitrary) Ewald parameter, and the sums run over the nonvanishing direct-lattice vectors $\mathbf{R}$ and the reciprocal-lattice vectors $\mathbf{G}$, respectively.

The convergence of $\tilde{E}(\Omega)$ with the supercell size is illustrated in Fig. 7 in the case of the diagonal Coulomb energy $J_{v,c}$. We see that even for the smallest supercell size considered here, corresponding to the supercell used in the solution of the single-particle problem, Eq. (11), the corrected energy $\tilde{E}$ has already converged to its asymptotic value (correspond-

ing to $\Omega \to \infty$). The expansion of Eq. (A3) works well whenever the electrostatic interaction between the periodic replicas of the quantum dots—described by the long-range part of the function $g(\mathbf{r}-\mathbf{r}')$—is essentially Coulombic. This includes the cases where the screening function $\overline{\epsilon}(\mathbf{r}-\mathbf{r}')$ of Eq. (12) is a constant or converges rapidly (within a few lattice constants) to its asymptotic ($|\mathbf{r}-\mathbf{r}'| \to \infty$) limit.

In the presence of strong ionic screening, however, the long-range part of $g(\mathbf{r}-\mathbf{r}')$ can deviate considerably from a simple $1/r$ function. In this case the corrected integrals (A3) converge slowly with the supercell size, particularly when $q_1 = q_2 = 1$. It is then more convenient to use a truncated form of the screened Coulomb interaction

$$g_{\text{cut}}(r) = \frac{g(r)}{1+\exp(|r-S_{\text{cut}}|/\lambda)}, \tag{A5}$$

where S_{cut} is a cutoff radius, and λ is a smoothing parameter (of the order of a few Å). Provided that (i) the cutoff radius S_{cut} is larger than the quantum-dot diameter D, and (ii) the supercell size is larger than $D+S_{\text{cut}}$, the truncated Coulomb potential effectively eliminates the electrostatic interactions between periodic replicas of the quantum dot, while correctly describing the intradot Coulomb and exchange interactions.

[1] R. S. Knox, Solid State Phys. **5**, 25 (1963).
[2] See, for example, A. P. Alivisatos, MRS Bull. **23**, 18 (1998); A. J. Nozik and O. I. Micic, *ibid.* **23**, 24 (1998).
[3] D. J. Norris and M. G. Bawendi, Phys. Rev. B **53**, 16 338 (1996).
[4] D. Bertram, O. I. Micic, and A. J. Nozik, Phys. Rev. B **57**, R4265 (1998).
[5] U. Banin, C. J. Lee, A. A. Guzelian, A. V. Kadavanich, A. P. Alivisatos, W. Jaskolski, G. W. Bryant, Al. L. Efros, and M. Rosen, J. Chem. Phys. **109**, 2306 (1998).
[6] D. J. Norris, Al. L. Efros, M. Rosen, and M. G. Bawendi, Phys. Rev. B **53**, 16 347 (1996).
[7] O. I. Micic, H. M. Cheong, H. Fu, A. Zunger, J. R. Sprague, A. Mascarenhas, and A. J. Nozik, J. Phys. Chem. B **101**, 4904 (1997).
[8] M. Nirmal, D. J. Norris, M. Kuno, M. G. Bawendi, Al. L. Efros, and M. Rosen, Phys. Rev. Lett. **75**, 3728 (1995).
[9] Al. L. Efros, M. Rosen, M. Kuno, M. Nirmal, D. J. Norris, and M. G. Bawendi, Phys. Rev. B **54**, 4843 (1996).
[10] M. Chamarro, C. Gourdon, P. Lavallard, O. Lublinskaya, and A. I. Ekimov, Phys. Rev. B **53**, 1336 (1996).
[11] U. Woggon, F. Gindele, O. Wind, and C. Klingshirn, Phys. Rev. B **54**, 1506 (1996).
[12] U. Banin, J. C. Lee, A. A. Guzelian, A. V. Kadavanich, and A. P. Alivisatos, Superlattices Microstruct. **22**, 559 (1997).
[13] S. A. Empedocles, D. J. Norris, and M. G. Bawendi, Phys. Rev. Lett. **77**, 3873 (1996).
[14] L. W. Wang and A. Zunger, J. Phys. Chem. B **102**, 6449 (1998).
[15] H. Fu and A. Zunger, Phys. Rev. B **57**, R15 064 (1998).
[16] A. Williamson and A. Zunger, Phys. Rev. B **59**, 15 819 (1999).
[17] Y. Z. Hu, M. Lindberg, and S. W. Koch, Phys. Rev. B **42**, 1713 (1990).
[18] E. Martin, C. Delerue, G. Allan, and M. Lannoo, Phys. Rev. B **50**, 18 258 (1994).
[19] K. Leung and K. B. Whaley, Phys. Rev. B **56**, 7455 (1997).
[20] K. Leung, S. Pokrant, and K. B. Whaley, Phys. Rev. B **57**, 12 291 (1998).
[21] M. Chamarro, M. Dib, V. Voliotis, A. Filoramo, P. Roussignol, T. Gacoin, J. P. Boilot, C. Delerue, G. Allan, and M. Lannoo, Phys. Rev. B **57**, 3729 (1998).
[22] A. Franceschetti and A. Zunger, Phys. Rev. Lett. **78**, 915 (1997).
[23] A. Franceschetti, L. W. Wang, H. Fu, and A. Zunger, Phys. Rev. B **58**, R13 367 (1998); A. Zunger, MRS Bull. **23**, 35 (1998).
[24] L. W. Wang and A. Zunger, Phys. Rev. B **51**, 17 398 (1995); H. Fu and A. Zunger, Phys. Rev. B **56**, 1496 (1997).
[25] A. Franceschetti and A. Zunger (unpublished).
[26] L. W. Wang and A. Zunger, J. Chem. Phys. **100**, 2394 (1994); J. Phys. Chem. **98**, 2158 (1994).
[27] L. W. Wang and A. Zunger, in *Semiconductor Nanoclusters*, edited by P. V. Kamat and D. Meisel (Elsevier, New York, 1996).
[28] L. J. Sham and T. M. Rice, Phys. Rev. **144**, 708 (1966).
[29] G. Strinati, Phys. Rev. B **29**, 5718 (1984).
[30] L. Hedin, Phys. Rev. **139**, A796 (1965).
[31] L. W. Wang and A. Zunger, Phys. Rev. Lett. **73**, 1039 (1994).
[32] L. C. Andreani, F. Bassani, and A. Quattropani, Lett. Nuovo Cimento **10**, 1473 (1988); K. Cho, Solid State Commun. **33**, 911 (1980).
[33] V. A. Kiselev and A. G. Zhilich, Fiz. Tverd. Tela (Leningrad) **14**, 1438 (1972) [Sov. Phys. Solid State **14**, 1233 (1972)]; **15**, 2024 (1972) [**15**, 1351 (1972)].
[34] R. Resta, Phys. Rev. B **16**, 2717 (1977).
[35] H. Haken, Lett. Nuovo Cimento **10**, 1230 (1956).
[36] Only the excitonic energy levels of the three largest InP nanocrystals are included in the fitting procedure.
[37] G. Makov and M. C. Payne, Phys. Rev. B **51**, 4014 (1995).
[38] K. Fuchs, Proc. R. Soc. London, Ser. A **151**, 585 (1935).